

Synergistic Development of Natural Rubber/Butyl Rubber Composites for Improved Interfacial Bonding and Enhanced Shock-Absorbing Capabilities

Yang Han, Hongbing Zheng, Yingxue Liu, Min Wang, Jiadong Wang, Qing Xie, Shuailin Jing, Xuan Qin,* and Liqun Zhang*



Cite This: *ACS Omega* 2024, 9, 13897–13905



Read Online

ACCESS |



Metrics & More

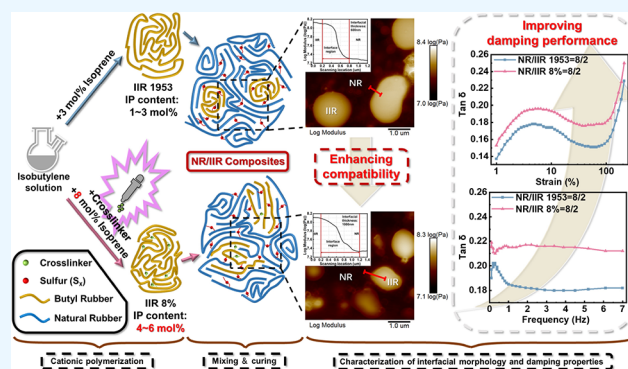


Article Recommendations



Supporting Information

ABSTRACT: Shock-absorbing materials play a vital role in various industrial sectors, including construction and transportation. Among these materials, natural rubber (NR) stands out due to its exceptional elastic and mechanical properties, coupled with its robust crack resistance. Nevertheless, with the rising demand for enhanced damping capacities, there is a need to further optimize the damping performance of NR. One direct approach is to blend it with high-damping rubber. Butyl rubber (IIR) is a prominent member of the high-damping rubber category. Integrating IIR effectively with the NR, however, presents challenges. These challenges arise from IIR's inherent characteristics, such as its low unsaturation, slower vulcanization rate, and restricted compatibility with NR. Addressing these challenges, our study employed isoprene and isobutene to synthesize a variant of butyl rubber with a higher degree of unsaturation—achieving an unsaturation level between 4 and 6 mol %. Notably, this heightened unsaturation significantly expedited the curing time of IIR and facilitated the concurrent vulcanization of both IIR and NR. Utilizing atomic force microscopy, we observed that the introduction of unsaturated double bonds ameliorated the compatibility between NR and IIR, leading to an interfacial region extending up to 1000 nm. Our tests using a dynamic mechanical analyzer and rubber processing analyzer demonstrated the material's damping temperature range. Furthermore, there was a noticeable rise in the loss factor ($\tan \delta$) at ambient temperature, which remains over 0.1 across both a frequency window of 0.2 to 5 Hz and a strain spectrum of 10 to 200%. This $\tan \delta$ enhancement ensured the potential of these rubber composites for shock-absorbing applications.



1. INTRODUCTION

The importance of shock absorption permeates many aspects of modern society. For instance, the aftermath of devastating earthquakes on structures such as buildings and bridges has spurred the construction industry to relentlessly innovate damping technologies and materials.^{1–3} In the realm of transportation, the automotive sector prioritizes frame materials that offer superior vibration isolation to mitigate the jolts and reverberations from road turbulence.⁴ This capacity not only improves driving comfort by buffering against road irregularities but also rapidly diminishes dynamic stress on vehicle components,⁵ thereby extending the vehicle's longevity. Rail transit, too, requires vibration isolation to adhere to seismic safety standards and to reduce train-induced disruptions to neighboring infrastructure.^{6,7} Aviation underscores the need for effective damping. Key areas such as pilot seats and landing gears are equipped to minimize disturbances from the engines and takeoff/landings to guarantee both pilots and passengers well-being.⁸ Intriguingly, places of creation, such as sports arenas and amusement parks, are not exempt—

they also abide by stringent shock absorption criteria to ensure safety.⁹ Furthermore, precision instruments universally treat vibration isolation and shock absorption as pivotal performance benchmarks for optimal performance.

At its core, shock absorption transforms kinetic energy mainly into heat, thereby reducing the kinetic force repercussions. Among the shock-absorbing materials, elastomers, especially rubber, take precedence. Subjected to cyclic loads, the elongation of molecular chains lags behind the applied stress, creating internal friction. This friction translates energy into dissipating heat, leading to effective energy management.¹⁰ In rubber-based dampers, the nonrubber

Received: November 12, 2023

Revised: February 10, 2024

Accepted: February 22, 2024

Published: March 13, 2024



segments primarily impart stiffness, while the rubber component contributes to strength and energy dissipation. Historically, enhancements in rubber dampers have come from two principal directions: optimizing structural design,¹¹ bolstering rubber's innate damping properties, like broadening damping temperature ranges and amplifying the loss factor. Combined together, these approaches ensure heightened conversion and dissipation of vibrational energy.

In various practical scenarios, the predominant rubber component within shock-absorbing materials is natural rubber (NR). This option is rooted not only in its cost-effectiveness but also in its outstanding stress-induced crystallization capability. This distinctive attribute is characterized by a low modulus under medium to low strain conditions, with a notable rise in modulus due to stress-induced crystallization at high strains.^{12,13} Consequently, NR delivers both mechanical resilience and resistance to damage.^{14,15} At the molecular level, NR boasts flexibility, characterized by its *cis*-1,4-isoprene main chain structure that benefits from minimal internal rotation barriers. This molecular architecture gives NR commendable elasticity, impact endurance, and resistance to permanent deformation, making it an exemplary shock absorber and buffer. However, its damping capacities under extreme events, such as vehicular collisions and earthquakes, call for further improvement. The inherent friction loss within NR during molecular chain movements results in a restricted damping temperature range and a suboptimal loss factor under ambient conditions. Addressing this shortcoming requires a material that mirrors NR's mechanical strengths, impact resistance, and crack growth resistance while also demonstrating superior damping traits. One solution lies in blending NR with rubber variants known for their damping prowess.^{16,17} This combination amplifies the beneficial characteristics of each component. For example, butyl rubber (IIR) is constructed primarily of isobutylene segments arranged head-to-tail, accompanied by spirally arranged, densely packed side methyl groups. Consequently, this structure endows the IIR with substantial steric hindrance, strong cohesion energy, and pronounced intramolecular friction. Literature has highlighted IIR's ability to maintain a $\tan \delta$ value over 0.6 across a wide temperature spectrum, establishing it as a premier damping material.¹⁸ Other benefits of IIR include crack growth resistance¹⁹ and impressive resistance to aging and corrosion.^{20,21} Notably, other rubber types featuring specific side-chain contents also demonstrate damping attributes. Examples encompass nitrile butadiene rubber,^{22,23} epoxy natural rubber,^{24,25} and chloroprene rubber.²⁶

Although IIR boasts impressive damping performance, it is not without its challenges. One key limitation is its scarcity of unsaturated double bonds, which are crucial for effective vulcanization. As a result, IIR often exhibits a slower vulcanization rate, presents bonding issues with other materials, and poses difficulties when blended or cocured with other rubber varieties.²⁷ When attempting to combine low-unsaturation IIR with NR to fabricate rubber damping materials, these challenges can hinder the desired enhancement in the overall damping performance of the resulting composite. To truly optimize the damping potential of such composites, a multifaceted strategy is imperative. It is essential to align the vulcanization rate of the IIR with that of the NR, ensuring that the remarkable damping attributes of butyl rubber remain intact. Equally crucial is enhancing the compatibility between the two rubber types.

Efforts aimed at enhancing the compatibility of NR matrix composites have predominantly revolved around adding small molecule compatibilizers, such as hindered phenols^{28,29} or small molecule damping materials. Li et al.³⁰ effectively bolstered the compatibility of NR and IIR blends through the synthesis of an isobutene (IB)–isoprene (IP) block copolymer. This ingenious method achieved an isoprene molar fraction of up to 14.5%, resulting in a composite suitable for high-damping isolation rubber bearings. Nevertheless, there is a noticeable gap in research regarding the optimization of IIR molecular chain structure to bolster its vulcanization rate and in situ compatibility with NR. The objective is to fine-tune the molecular chain structure to make it more compatible with NR, increase its double bond content for effective vulcanization, while still predominantly consisting of isobutylene. This multifaceted target could be approached in two main ways.

1. Refining the initiation system: This approach precisely controls over the initiation process, particularly by controlling the polymer end group during polymerization. By modulating the rate of carbocation polymerization, it is likely to minimize untimely transfer reactions, chain terminations, or other unintended side reactions.^{31–33}
2. Modifying the second monomer: By retaining IIR's main chain structure while introducing distinct side and end group configurations via diverse second monomers, direct introduction of double bonds becomes feasible. Examples include incorporating methyl and benzene structures. Such adjustment can also diminish the cationic acidity of allyl, thereby reducing chain transfer reactions with monomers or solvents.³⁴ Meanwhile, adding a specific amount of cross-linking agent during polymerization can both increase the product's molecular weight and stabilize copolymer properties.³⁵

This research embarks on highly unsaturated butyl rubber, distinguished by a significantly high IP binding content. Drawing from the pioneering work on low unsaturated butyl rubber, namely, IIR 1953 by Shandong Chambroad Sinopoly New Materials Co., Ltd., our approach introduces minimal quantities of cross-linking agents, specifically 1,5-hexadiene (Hex) and divinylbenzene (DVB). These agents are employed to fine-tune the structure and density of the cross-linking network. Our research critically examines the mechanical and damping characteristics of IIR and NR/IIR composites, both prior to and subsequent to structural adjustment. The overarching goal is to devise a straightforward methodology for crafting NR/IIR composites that are excellent shock-absorbing materials.

2. EXPERIMENTAL SECTION

2.1. Materials. IIR 1953, a key component of this study, was supplied by Shandong Chambroad Sinopoly New Materials Co., Ltd. NR (smoked sheet #1) component was purchased from Nanjing Shengdong Chemical Co., Ltd. (Nanjing, China), while 1–5 hexadiene and divinylbenzene came from Aladdin Biochemical Technology Co., Ltd. (Shanghai, China). Other chemicals and ingredients were procured from various Chinese suppliers and were used as received without additional purification.

2.2. Sample Preparation. **2.2.1. Synthesis of Highly Unsaturated IIR.** Polymerization was conducted in a nitrogen-

saturated glovebox with a low-temperature cold bath, ensuring optimal conditions ($[\text{H}_2\text{O}] < 1.0 \times 10^{-6}$, $[\text{O}_2] < 1.0 \times 10^{-6}$). With liquid nitrogen, the temperature was maintained at -95 °C. The monomer, IB, had a concentration of 15 wt %, with chloromethane (CH_3Cl) serving as the solvent. The process involved adding a CH_3Cl solution of IB, followed by IP, cross-linking agent, and finally a CH_2Cl_2 solution of the initiator. The reaction was terminated by using ethanol.

The sample naming and corresponding polymerization conditions:

IIR 1953: provided by Shandong Chambroad Sinopoly New Materials Co., Ltd.

IIR 8%: nIB/nIP = 92/8, with no cross-linking agent.

IIR 8%-Hex: nIB/nIP = 92/8, with 1,5-hexadiene (/IB wt % = 0.4) as a cross-linking agent.

IIR 8%-DVB: nIB/nIP = 92/8, with divinylbenzene (/IB wt % = 0.4) as a cross-linking agent.

2.2.2. Preparation of the IIR Compound. The raw IIR material underwent kneading on a Φ 152.4 mm two-roll mill for 3 min at ambient temperature. It was subsequently combined with additives: 3.0 phr of zinc oxide, 1.0 phr of stearic acid, 1.0 phr of accelerant TMTD (tetramethylthiuram disulfide), 50 phr of carbon black, and 1.75 phr of sulfur. The resulting mixture was further kneaded on the two-roll mill for another 5 min at room temperature, culminating in the formation of the IIR compound. Following this procedure, the compounds were subjected to hot pressing and vulcanization at 160 °C under a pressure of 15 MPa. The optimal cure time, vital for optimal vulcanization, was determined by using a disc rheometer.

2.2.3. Preparation of NR/IIR Composites. The initial IIR was first kneaded for 3 min on a Φ 152.4 mm two-roll mill at room temperature. Once kneaded, it was blended with additives comprising 3.2 phr of zinc oxide, 1.2 phr of stearic acid, 1.6 phr of antioxidant 4010NA (1,4-benzenediamine), 0.36 phr of accelerant TMTD (tetramethylthiuram disulfide), 0.96 phr of accelerant CZ (*N*-cyclohexyl-2-benzothiazole sulfonamide), 0.12 phr of accelerant M (2-mercaptobenzothiazole), 50 phr of carbon black, and 1.2 phr of sulfur. Following this procedure, the mixture was subjected to an additional kneading phase on the two-roll mill at room temperature for 5 min to produce the IIR mixture.

Likewise, the NR preparation mirrored the IIR process: the raw NR was kneaded, blended with an identical set of additives, and underwent an additional kneading phase, culminating in the NR mixture. Finally, the mixture was kneaded on the two-roll mill at room temperature for 5 min to form the IIR mixture. The ultimate NR/IIR composites were formulated in varying mass ratios of 9/1, 8/2, 7/3, and 6/4. After blending, each composite was kneaded for 5 min on a two-roll mill at room temperature, then hot pressed, and vulcanized at 145 °C under 15 MPa pressure. The duration of this process aligned with the optimum cure times derived from a disc rheometer.

2.3. Characterization. The proton nuclear magnetic resonance (^1H NMR) spectra of IIR were acquired using deuterated chloroform (CDCl_3) as the solvent, measured with a Bruker AV400 spectrometer at room temperature. The analysis operated at a resonant frequency of 400 MHz. Furthermore, the degree of unsaturation within the IIR sample was quantified by using eq 1:

$$U_{\text{mol}\%} = \frac{A_{5.07}}{A_{5.07} + \frac{A_{1.11}}{6}} \times 100\% \quad (1)$$

where A_δ denotes the peak area corresponding to the chemical shift δ . In the obtained ^1H NMR spectra, specific peaks held significance. The resonance at 5.07 ppm represents the hydrogen bonded to the allyl carbon in IP segment, with each hydrogen equating to a mole of IP. Conversely, the 1.11 ppm reflects the hydrogen of the side methyl ($-\text{CH}_3$) group of the IB segment, where every six moles of hydrogen atoms correspond to one mole of IB.

For molecular weight analysis of the initial IIR sample, we employed gel permeation chromatography (GPC) using a Waters Breeze instrument. The setup consisted of three water columns and incorporated a Waters 2410 refractive index detector. Tetrahydrofuran served as the eluent, maintaining a flow rate of 1 mL/min.

The synthesized IIR samples underwent Fourier transform infrared (FTIR) spectroscopy analysis using a TENSOR 27 FTIR from Bruker, Germany. Scans were conducted in the wavenumber range 4000 to 400 cm^{-1} utilizing the KBr pellet technique with a resolution of 4 cm^{-1} .

We evaluated the cure characteristics of rubber compounds with a P3555B2 Disc Vulkameter from the Beijing Huanfeng Chemical Machinery Trial Plant, Beijing, China. This assessment aligned with the ISO 3417-2008 standards, examining the IIR compounds at 160 °C and the NR/IIR composites at 145 °C.

Thermal properties were assessed by using differential scanning calorimetry (DSC) on a DSC1 instrument from Mettler-Toledo International, Inc. This analysis spanned a temperature range from -100 to 100 °C, under a nitrogen atmosphere, and progressed at a rate of 10 °C/min across.

For mechanical properties, a CMT4104 instrument from SANS Testing Machine Co. was utilized, following ASTM D638 standards. Tests were executed under ambient conditions with a pace of 500 mm/min.

To determine dynamic viscoelasticity, DMA measurements on a DMA1 from Mettler-Toledo International, Inc. were undertaken, spanning a temperature range from -80 to 100 °C and progressing at 3 °C/min. The chosen frequency and strain amplitude were 10 Hz and 0.3%, respectively, with DMA specimens measuring 20 mm long, 6 mm wide, and 2 mm thick.

Damping performance of the NR/IIR composites was studied using a rubber process analyzer from RPA 2000, Alpha Technologies, USA. Strain sweeps varied from 1 to 300% at 40 °C with a 1 Hz frequency, while frequency sweeps ranged from 0.1 to 7 Hz at 40 °C under a consistent strain of 100%.

Finally, surface morphology was elucidated using an atomic force microscope (AFM) on a MultiMode8 AFM from Bruker. Prior to the test, sample surfaces were prepared via freezing polishing on an EM UC7 ultramicrotome (Leica) at -110 °C. Measurements in the Peak Force-Quantitative Nanomechanical Mapping (PF-QNM) mode employed a default amplitude of 150 nm and a RESTPA-300 cantilever with a 40 N/m spring constant. Data was collected from randomly selected $10 \times 10 \mu\text{m}^2$ and $5 \times 5 \mu\text{m}^2$ surfaces with a 256×256 -pixel resolution.

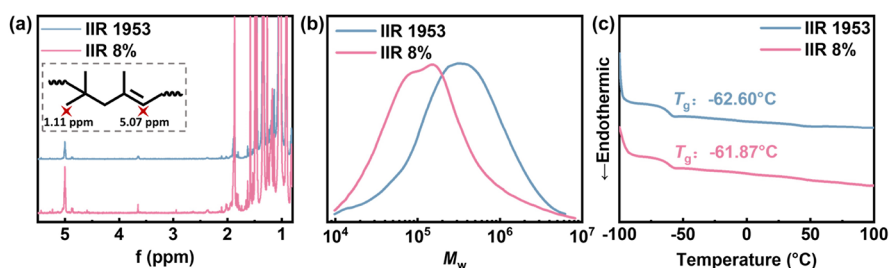


Figure 1. (a) ^1H NMR nuclear spectra of IIR with different unsaturation. (b) GPC curve of IIR with different unsaturation. (c) DSC curve of IIR with different unsaturation.

3. RESULTS AND DISCUSSION

3.1. Structural Characterization of As-Received Butyl Rubber. To thoroughly analyze butyl rubber with varying unsaturation levels, specifically the IIR with 8% unsaturation and the IIR 1953, we employed various characterization techniques, including ^1H NMR, GPC, and DSC. Figure 1 provides a visual representation of the outcomes of these analyses.

The ^1H NMR nuclear spectra, illustrated in Figure 1a, underscore the effective augmentation of unsaturation. The peak identified at 5.07 ppm corresponds to the hydrogen attached to the allyl carbon within the IP unit of IIR. Equation 1 enables the calculation of IP's relative content. Notably, as the IP dosage escalates, there is a corresponding increase in the IP binding content within the as-received rubber. This phenomenon results in a pronounced increase in unsaturation, thereby enhancing the corresponding peak area. Analyzing the GPC curve illustrated in Figure 1b reveals a discernible pattern: an uptick in IP binding content is inversely proportional to the molecular weight of the initial IIR. Such behavior can be traced back to the protons generated by active centers during polymerization. As the IP content swells, these protons are more susceptible to chain transfer and termination as the IP content increases. Consequently, this impedes the extension of the molecular length. Moving on to the DSC results presented in Figure 1c, it is evident that the heightened unsaturation does not affect the glass transition temperature (T_g) of the original rubber, both of which hover around -62°C . This consistency results from T_g being intrinsically determined by the molecular structure, directly linked to the flexibility of the molecular chain. The increase in IP content within the main chain structure exclusively elevates the presence of the isolated double bond structures, leaving the molecular chain's flexibility unaltered.

To delve deeper, two distinct cross-linking agents were incorporated, producing IIR 8%-Hex and IIR 8%-DVB, both derivatives of IIR 8%. Through FTIR spectroscopy, the four IIR as-received rubber variants were analyzed with the results presented in Figure 2.

In Figure 2, the absorption peaks provide insights into the structure of the IIR. The peaks registered at 2953 and 2924 cm^{-1} are attributed to the asymmetric stretching vibrations of the $-\text{CH}_3$ and $-\text{CH}_2$ groups, which are present in both IB and IP segments. Furthermore, the peak situated at 2851 cm^{-1} represents the symmetric stretching vibration of the $-\text{CH}_3$ and $-\text{CH}_2$ groups. Notably, the peak at 1633 cm^{-1} is indicative of the stretching vibration of the carbon-carbon double bond ($-\text{C}=\text{C}-$), which primarily originates from the IP unit within the IIR. This intensity of this particular peak serves as a testament to the increase in the IP binding content. Such

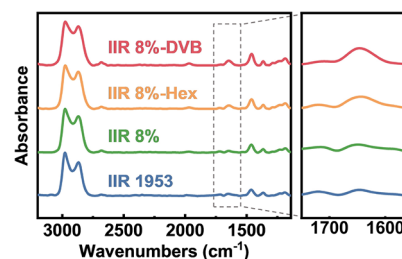


Figure 2. FTIR spectra of IIR with different unsaturation and cross-linking agents.

observations confirm that the structure formed due to the introduction of the cross-linking agent does not diminish the unsaturation levels of the as-received rubber when comparable IP dosages are used.

3.2. Characterization of Curing Properties and Dynamic and Static Mechanical Properties of Vulcanized IIR. To elucidate the implications of increased unsaturation on the vulcanization behavior of the IIR, a detailed examination was conducted. Four distinct IIR variants were subjected to a vulcanization process, the results of which are visually represented in Figure 3a. To comprehensively understand the consequences of enhanced unsaturation and the ensuing transformation of the cross-linking network structure, both dynamic and static mechanical properties were analyzed. The findings of these evaluations are depicted in Figure 3b,c, respectively. It is noteworthy that the additional vulcanization characteristics and mechanical properties can also be cross-referred in Tables S1 and S2.

Notably, as depicted in Figure 3a and Table S1, the conspicuous increase in unsaturation resulting from the surge in IP binding content markedly influences the optimum cure time. This observation suggests that an increase in IP binding content can effectively shorten the IIR's optimum cure time, aligning it with the vulcanization pace of NR. Interestingly, changes in the double bond content and cross-linking network structure exert no visible effect on the torque difference (ΔM). The stress-strain curves, as showcased in Figure 3b and summarized in Table S2, provide further insights. In comparison with IIR 1953, IIR 8% demonstrates a higher modulus. Conversely, IIR 8%-DVB, due to the presence of a rigid short-chain benzene ring within the cross-linking network, boasts the highest modulus. Such a feature renders the network more condensed and robust, thereby bolstering the resistance against molecular chain deformation. As the IP binding content ascends, there is a noticeable enhancement in the density of the cross-linking network, culminating in a subsequent dip in elongation. Figure 3c delineates the temperature-relative loss factor curves of the various IIR

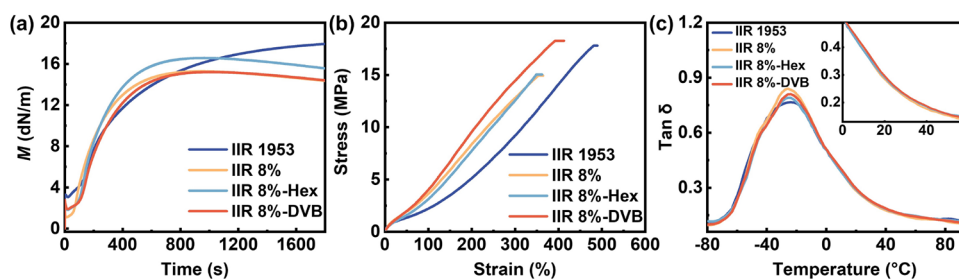


Figure 3. (a) Curing curves of the IIR at 160 °C. (b) Stress–strain curves of IIR. (c) Loss factor–temperature curves of IIR.

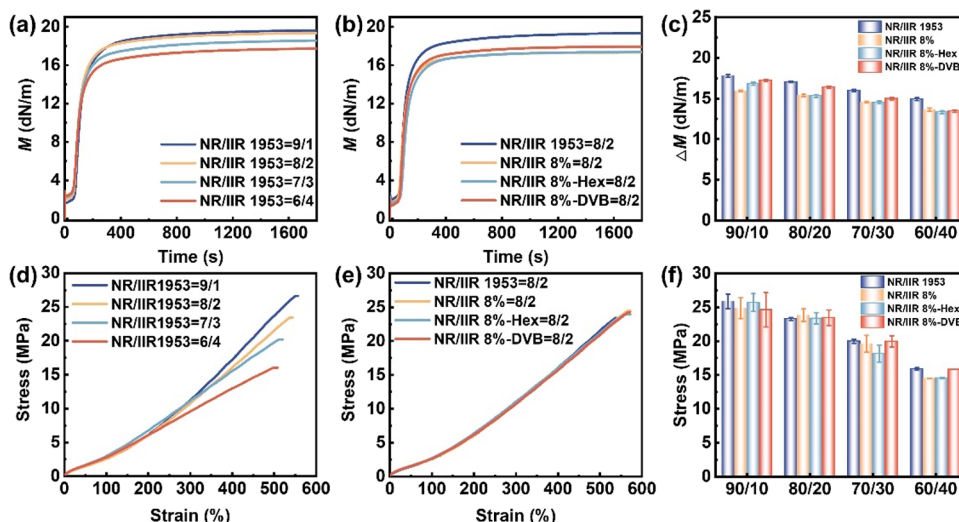


Figure 4. (a) Curing curves of NR/IIR 1953 composites with different blending ratios at 145 °C (9/1, 8/2, 7/3, and 6/4). (b) Curing curves of NR/IIR (8/2) composites at 145 °C. (c) Torque difference (ΔM) of various NR/IIR composites. (d) Stress–strain curves of NR/IIR 1953 composites with different blending ratios (9/1, 8/2, 7/3, and 6/4). (e) Stress–strain curves of NR/IIR (8/2) composites. (f) Tensile strength of various NR/IIR composites.

formulations. There are subtle discrepancies in the peak values of the loss factor. The effective damping temperature range (where $\tan \delta > 0.3$)^{36,37} spans from approximately -57 to 20 °C. Remarkably, the $\tan \delta$ values at room temperature remain fairly consistent, implying that the inherent damping properties of pure IIR are predominantly governed by the abundant side methyl structure of IB. Therefore, a marginal uptick in IP binding content does not significantly perturb the overarching damping characteristics of IIR.

3.3. Vulcanization Properties and Static Mechanical Properties Characterization of NR/IIR Composites. In this section, we closely examined the vulcanization behaviors and the static mechanical properties of NR/IIR composites, which are crafted by integrating NR with four unique IIR variants. The derived insights are graphically represented in Figure 4, respectively. For an in-depth understanding, additional data on vulcanization characteristics and mechanical properties can be found in Tables S3 and S4.

For instance, NR/IIR 1953 is considered in Figure 4a, where NR integrates with a consistent type of IIR. Within this context, the torque difference (ΔM) steadily diminishes as the proportion of the IIR ingredient rises. Such a decrease is indicative of NR's superior overall performance relative to that of IIR. Likewise, the stress–strain curve depicted in Figure 4d directly underscores that the composite's mechanical attributes are enhanced with the escalating content of the NR component. A similar pattern can be discerned in Figure 4f. Reviewing the same blend ratio, as visualized in Figure 4b,c, it

is intriguing that ΔM remains rather stable despite increasing the level of IIR unsaturation. This phenomenon largely results from the reduction in the IIR molecular weight stemming from intensified unsaturation, as illustrated in Figure 1b. Moreover, when juxtaposing mechanical characteristics at an identical blending ratio, an unanticipated propensity emerges. Contrary to the differentiated mechanical traits of the four IIRs portrayed in Figure 3b, their amalgamation with NR yields remarkably consistent mechanical outcomes across diverse composite materials, given the same blending ratio. Such revelation intimates that the composite methodology not only capitalizes on NR's extraordinary mechanical properties and bequeaths them to IIR but also extends to the holistic composite material.

3.4. Microphase Structure and Compatibility Characterization NR/IIR Composites. Peak force quantitative nanomechanical mapping (PF-QNM) technique, a fusion of atomic force microscopy (AFM) with peak force tapping mode, emerges as a pivotal tool for characterizing the interface traits of polymer composites.^{38–40} Unlike its predecessors, the conventional tapping mode, the PF-QNM mode offers enhanced accuracy and precision in evaluating interfacial interaction forces and the associated thickness. Leveraging this methodology,^{41,42} it becomes feasible to precisely analyze variations in the modulus of rubber blends within the two-phase and interfacial regions through AFM. Subsequently, the thickness of the interfacial region can be quantitatively computed through Young's modulus. Particularly, at an NR/

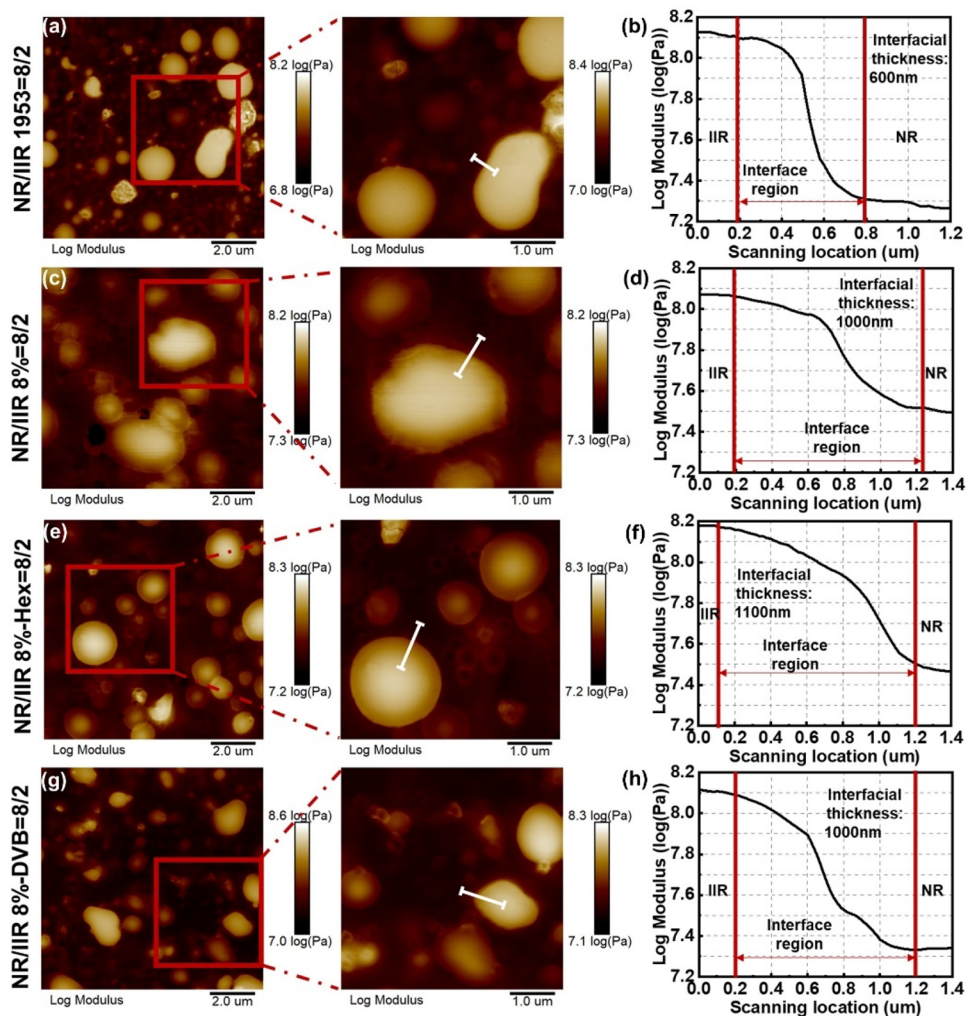


Figure 5. (a–h) Representative AFM Young's modulus images of NR/IIR (8/2) composites and their corresponding modulus–scanning location curves to represent the interfacial region thickness between NR and IIR.

IIR blend ratio of 8/2, the AFM Young's modulus imaging effectively captures the two-phase separation along with their neighboring interfacial zones, as vividly delineated in Figure 5 and Figure S1.

AFM images present the typical sea island morphology of the NR/IIR composites. Upon juxtaposing the NR/IIR 8% composites with NR/IIR 1953, distinctive characteristics manifest. The interfacial region in the three NR/IIR 8% composites stands out, showcasing an amplified interfacial thickness. Translating this phenomenon into a modulus–scanning location curve reveals that the interfacial region thickness within the NR/IIR 1953 composite clocks in at 600 nm. Intriguingly, this interfacial region demonstrates a steeper slope compared to the rest, indicating a swift transition in the modulus at the biphasic interface. Such a stark shift alludes to feeble interfacial bonding, thus potentially undermining the damping dissipation efficiency and energy transmission. Conversely, Figure 5d reveals that the NR/IIR 8% composite's interfacial region thickness is extending to 1000 nm, accompanied by a gradual modulus change across the two phases. It is noteworthy that the introduction of two distinct cross-linking agents retains the interfacial thickness within the range from 1000 to 1100 nm. Such a consistent outcome further reinforces the proposition that augmenting the IP

binding content in the IIR inherently fortifies the interfacial bonding of NR/IIR composites, promoting stress transfer between the continuous phase and the dispersed phase. Moreover, any alteration of the cross-linking network structure, grounded in this premise, seems not to compromise the blend's compatibility.

3.5. Dynamic Mechanical Properties Characterization of NR/IIR Composites.

The insights from AFM characterization highlight that the damping properties of NR/IIR composites are not merely the additive outcomes of their individual components, especially when contrasted with the behavior of pure IIRs. A pronounced disparity in cohesion energy and thermodynamic compatibility arises due to the inherent structural difference in molecular chains between NR and the less unsaturated IIR. This divergence is visually discernible in the stark boundary between the two phases visible at the microscale morphology. Unlike pure IIRs, there is no prominent interfacial region contributing to the energy transfer and damping dissipation. However, the incorporation of highly unsaturated IIR brings about a transformative change. This variant, due to its reduced vulcanization time and enhanced compatibility with NR, mends the aforementioned structural and cohesive disparities. To provide a direct assessment of the damping performance, we characterized

the dynamic mechanical properties of NR/IIR composites. Figure 6 illustrates the temperature-dependent $\tan \delta$ curves of the four distinct NR/IIR composites. These variations were informed by blending ratio that spanned from 9/1 to 6/4.

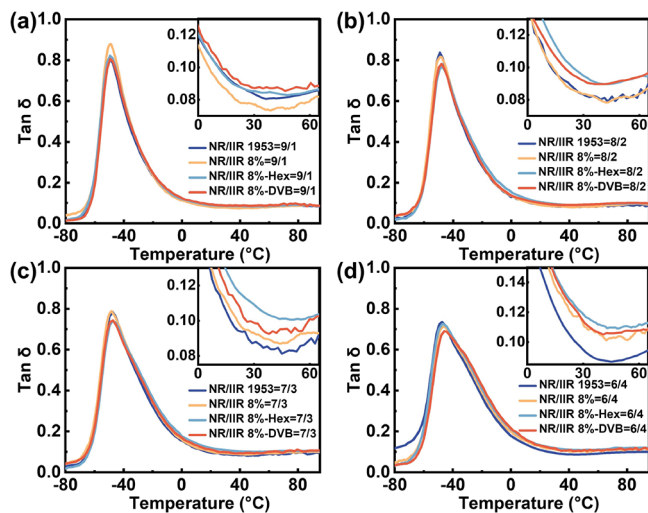


Figure 6. Loss factor–temperature curves of NR/IIR composites with different blending ratios: (a) 9/1, (b) 8/2, (c) 7/3, and (d) 6/4.

In comparison to Figure 3c where the $\tan \delta$ peak of pure IIR rests approximately at -33 °C, Figure 6 and Figure S2 unveil that the $\tan \delta$ peak of NR/IIR composites progressively shifts toward warmer temperatures as the blending ratio diminishes. This propensity indicates a higher proportion of IIR components content in the composites, and this alteration effectively extends the functional damping temperature range of NR/IIR composites from an initial -57 to -24 °C to a broader -57 to -10 °C. This broadened range emphasizes a marked improvement in the damping performance over pure NR.

Although the peak value of $\tan \delta$ of NR/IIR composites subtly decreased with the increase in IIR content, the loss factor at room temperature experiences a consistent accent. More notably, the loss factors for NR/IIR 8%-Hex and NR/IIR 8%-DVB outpace those of NR/IIR 1953 and NR/IIR 8%. Given the augmented IP content in IIR 8% relative to IIR 1953, its molecular chain structure bears a greater resemblance to that of NR. This alignment facilitates a more coordinated energy transfer and damping dissipation between the two phases of the composite, resulting in a synchronized molecular chain movement and superior thermodynamic compatibility. This observation aligns seamlessly to the more congruent NR co-curing rate depicted in Figure 3a and is reaffirmed by the insights drawn from the AFM phase diagram in Figure 5.

Corroborating the conclusions from Figure 3c, which posit that increased unsaturation does not compromise the IIR's damping performance, Figures 5 and 6 collectively showcase that an IIR variant with superior compatibility with NR delivers enhanced damping performance to the composite. The strategic inclusion of 1,5-hexadiene as a cross-linking agent further magnifies the cross-linking density, rendering the cross-linking network more akin to NR. Therefore, the NR/IIR 8%-Hex composite manifests the lowest $\tan \delta$ peak value and the highest room temperature loss factor, characteristics that correspond to the broadest interfacial region thickness observed in Figure 5c. In contrast, NR/IIR 1953 demonstrates

the narrowest damping temperature spectrum and the lowest loss factor of room temperature, in agreement with the AFM observations of its most slender interfacial region and its acute two-phase modulus slope shift. Collectively, these findings accentuate the pivotal role of heightened IIR unsaturation in securing a more seamless compatibility with the NR, leading to a more conspicuous two-phase interfacial region and an improved transfer of two-phase interaction forces between phases. As a result, IIR's inherent damping capabilities are optimally harnessed in the composite blends. Moreover, the integration of a cross-linking agent, coupled with the elevation of IIR unsaturation, not only cements this compatibility but also accentuates the damping performance.

To elucidate the potential applications of a heightened IP binding content in the IIR in enhancing the damping efficacy of NR/IIR composites, we embarked on RPA tests. The tests were meticulously designed to assess the damping properties of the NR/IIR composites under conditions of dynamic shear strain and dynamic frequency. The insights gleaned from the RPA experiments are visually encapsulated in Figure 7.

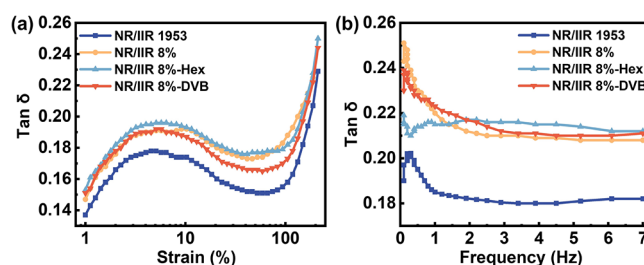


Figure 7. (a) Loss factor–dynamic strain curves. (b) Loss factor–dynamic frequency curves.

In our study focusing on the NR/IIR blending with an 80/20 ratio, the heightened unsaturation of IIR imparts an overall rise in the $\tan \delta$ of the blend, a finding that aligns with the results of DMA and AFM examinations. This outcome indicates that the augmented IIR unsaturation bolsters the interfacial bonding strength, leading to increased frictional loss during movement and thus effective energy dissipation. According to ISO standards, elastomers that maintain with a $\tan \delta$ exceeding 0.1 across a frequency range from 0.2 to 5 Hz and strain range from 10 to 200% are prime candidates for vibration isolation rubber bearings.

In essence, enhancing the IP unit content in IIR and incorporating a cross-linking agent with a structure akin to the vulcanized rubber cross-linking network can lead to the straightforward creation of high-performance NR/IIR composites. These advanced composites, marked by their exceptional damping attributes, emerge as potential contenders as shock-absorbing materials.

4. CONCLUSIONS

In this study, a successful synthesis of butyl rubber with unsaturation levels of 4 to 6 mol % was achieved. Analysis via the curing curve and DMA test has revealed that the enhanced unsaturation effectively reduces the curing process of IIR, all the while maintaining its intrinsic damping performance. Additionally, the inclusion of a rigid short-chain structure in the cross-linking network augments the modulus. AFM modulus mapping image substantiates the marked compatibility enhancements within NR/IIR composites. Notably, at an

80/20 blending ratio, the interfacial region thickness observed a leap from 600 to 1000 nm, showcasing a discernible morphology. This morphological adjustment was paralleled to the uplifted damping attributes in the NR/IIR composites. With the damping temperature range stretching to 47 °C and their $\tan \delta$ values at room temperature surpassing 0.1, these composites demonstrated commendable shock absorption qualities. Given that the $\tan \delta$ values also consistently remain over 0.1 across a frequency window of 0.2 to 5 Hz and a strain spectrum of 10 to 200%, the potential of these rubber formulations for shock-absorbing applications is undeniable. This study sets a precedent in the realm of high-performance, shock-absorbing NR/IIR composites.

■ ASSOCIATED CONTENT

SI Supporting Information

The Supporting Information is available free of charge at <https://pubs.acs.org/doi/10.1021/acsomega.3c08996>.

Detailed cure characteristics and static mechanical properties of IIR samples; detailed cure characteristics and static mechanical properties of NR/IIR composites; Young's modulus images of NR/IIR (8/2) composites and their corresponding modulus–scanning location curves; loss factor–temperature curves of NR/IIR composites (PDF)

■ AUTHOR INFORMATION

Corresponding Authors

Xuan Qin – State Key Laboratory of Organic–Inorganic Composites, Beijing University of Chemical Technology, Beijing 100029, China; Engineering Research Center of Elastomer Materials Energy Conservation and Resources, Ministry of Education, Beijing 100029, China; Email: qinxuan@mail.buct.edu.cn

Liqun Zhang – State Key Laboratory of Organic–Inorganic Composites, Beijing University of Chemical Technology, Beijing 100029, China; Engineering Research Center of Elastomer Materials Energy Conservation and Resources, Ministry of Education, Beijing 100029, China; Institute of Emergent Elastomers, School of Materials Science and Engineering, South China University of Technology, Guangzhou, Guangdong 510640, China; orcid.org/0000-0002-2103-6294; Email: zhanglq@mail.buct.edu.cn

Authors

Yang Han – State Key Laboratory of Organic–Inorganic Composites, Beijing University of Chemical Technology, Beijing 100029, China; Engineering Research Center of Elastomer Materials Energy Conservation and Resources, Ministry of Education, Beijing 100029, China

Hongbing Zheng – State Key Laboratory of Organic–Inorganic Composites, Beijing University of Chemical Technology, Beijing 100029, China; Shandong Chambroad Sinopoly New Materials Co., Ltd., Binzhou 256500, China

Yingxue Liu – State Key Laboratory of Organic–Inorganic Composites, Beijing University of Chemical Technology, Beijing 100029, China; Engineering Research Center of Elastomer Materials Energy Conservation and Resources, Ministry of Education, Beijing 100029, China

Min Wang – State Key Laboratory of Organic–Inorganic Composites, Beijing University of Chemical Technology,

Beijing 100029, China; Engineering Research Center of Elastomer Materials Energy Conservation and Resources, Ministry of Education, Beijing 100029, China; orcid.org/0000-0003-0170-7449

Jiadong Wang – State Key Laboratory of Organic–Inorganic Composites, Beijing University of Chemical Technology, Beijing 100029, China; Engineering Research Center of Elastomer Materials Energy Conservation and Resources, Ministry of Education, Beijing 100029, China

Qing Xie – Shandong Chambroad Sinopoly New Materials Co., Ltd., Binzhou 256500, China

Shuailin Jing – Shandong Chambroad Sinopoly New Materials Co., Ltd., Binzhou 256500, China

Complete contact information is available at:

<https://pubs.acs.org/10.1021/acsomega.3c08996>

Notes

The authors declare no competing financial interest.

■ ACKNOWLEDGMENTS

This work was supported by the National Key R&D Program of China (2022YFB3704700) and the National Science Foundation for Young Scientists of China (52003016).

■ REFERENCES

- (1) Jankowski, R.; Wilde, K.; Fujino, Y. Reduction of pounding effects in elevated bridges during earthquakes. *Earthquake Engineering & Structural Dynamics* **2000**, *29* (2), 195–212.
- (2) Murota, N.; Mori, T. An Experimental Study on Scale Effect in Dynamic Shear Properties of High-Damping Rubber Bearings. *Front. Built Environ.* **2020**, *6*, 37.
- (3) Zhang, R.-j.; Li, A.-q. Experimental study on temperature dependence of mechanical properties of scaled high-performance rubber bearings. *Composites Part B: Engineering* **2020**, *190*, No. 107932.
- (4) Jeon, S.; Shen, B.; Traugott, N. A.; Zhu, Z.; Fang, L.; Yakacki, C. M.; Nguyen, T. D.; Kang, S. H. Synergistic Energy Absorption Mechanisms of Architected Liquid Crystal Elastomers. *Adv. Mater.* **2022**, *34* (14), 2200272.
- (5) Silveira, M.; Pontes, B. R.; Balthazar, J. M. Use of nonlinear asymmetrical shock absorber to improve comfort on passenger vehicles. *Journal of Sound and Vibration* **2014**, *333* (7), 2114–2129.
- (6) Long, X.-H.; Ma, Y.-T.; Yue, R.; Fan, J. Experimental study on impact behaviors of rubber shock absorbers. *Construction and Building Materials* **2018**, *173*, 718–729.
- (7) Han, S.; Chen, F.; Yu, Y.; Zheng, Z.; Chen, L.; Wang, G. Bamboo-Inspired Renewable, Lightweight, and Vibration-Damping Laminated Structural Materials for the Floor of a Railroad Car. *ACS Appl. Mater. Interfaces* **2022**, *14* (37), 42645–42655.
- (8) Ilić, Z.; Rašuo, B.; Jovanović, M.; Jovičić, S.; Tomić, L.; Janković, M.; Petrašinović, D. The Efficiency of Passive Vibration Damping on the Pilot Seat of Piston Propeller Aircraft. *Measurement* **2017**, *95*, 21–32.
- (9) Huang, T. J.; Chang, L. T. Design and evaluation of shock-absorbing rubber tile for playground safety. *Materials & Design* **2009**, *30* (9), 3819–3823.
- (10) Markou, A. A.; Manolis, G. D. Mechanical models for shear behavior in high damping rubber bearings. *Soil Dynamics and Earthquake Engineering* **2016**, *90*, 221–226.
- (11) Pan, P.; Shen, S.; Shen, Z.; Gong, R. Experimental investigation on the effectiveness of laminated rubber bearings to isolate metro generated vibration. *Measurement* **2017**, *122*, 554 DOI: [10.1016/j.measurement.2017.07.019](https://doi.org/10.1016/j.measurement.2017.07.019).
- (12) Toki, S.; Sics, I.; Ran, S.; Liu, L. Z.; Hsiao, B.; Murakami, S.; Senoo, K.; Kohjiya, S. New Insights into Structural Development in

Natural Rubber during Uniaxial Deformation by In Situ Synchrotron X-ray Diffraction. *Macromolecules* **2002**, *35* (17), 6578–6584.

(13) Brüning, K.; Schneider, K.; Roth, S. V.; Heinrich, G. Kinetics of Strain-Induced Crystallization in Natural Rubber Studied by WAXD: Dynamic and Impact Tensile Experiments. *Macromolecules* **2012**, *45* (19), 7914–7919.

(14) Xu, Z.; Lu, Y.; Zhang, L.; Yan, S. Characterization methods and research progresses for stretching orientation and strain-induced crystallization of elastomers. *Acta Polym. Sin.* **2011**, *11* (6), 586–595.

(15) Chen, X.; Meng, L.; Zhang, W.; Ye, K.; Xie, C.; Wang, D.; Chen, W.; Nan, M.; Wang, S.; Li, L. Frustrating Strain-Induced Crystallization of Natural Rubber with Biaxial Stretch. *ACS Appl. Mater. Interfaces* **2019**, *11* (50), 47535–47544.

(16) Chen, B.; Dai, J.; Song, T.; Guan, Q. Research and Development of High-Performance High-Damping Rubber Materials for High-Damping Rubber Isolation Bearings: A Review. *Polymers* **2022**, *14* (12), 2427.

(17) Weng, G.; Huang, G.; Qu, L.; Nie, Y.; Wu, J. Large-Scale Orientation in a Vulcanized Stretched Natural Rubber Network: Proved by In Situ Synchrotron X-ray Diffraction Characterization. *Journal of physical chemistry. B* **2010**, *114* (21), 7179–7188.

(18) Dall'Asta, A.; Ragni, L. Nonlinear Behavior of Dynamic Systems with High Damping Rubber Devices. *Engineering Structures* **2008**, *30* (12), 3610–3618.

(19) Gent, A. N.; Zhang, L. Strain-Induced Crystallization and Strength of Rubber. *Rubber Chem. Technol.* **2002**, *75* (5), 923–934.

(20) White, J. L.; Shaffer, T. D.; Ruff, C. J.; Cross, J. P. Incorporation of Isoprene in Isobutylene/Isoprene Copolymers: NMR Identification of Branching in Butyl Rubber. *Macromolecules* **1995**, *28* (9), 3290–3300.

(21) Guerrero, A.; Kulbaba, K.; Bochmann, M. Alkyl Zinc Chlorides as New Initiators for the Polymerization and Copolymerization of Isobutene. *Macromol. Chem. Phys.* **2008**, *209* (16), 1714–1720.

(22) Qiao, B.; Zhao, X.; Yue, D.; Zhang, L.; Wu, S. A combined experiment and molecular dynamics simulation study of hydrogen bonds and free volume in nitrile-butadiene rubber/hindered phenol damping mixtures. *J. Mater. Chem.* **2012**, *22* (24), 12339–12348.

(23) Zhao, X.; Yang, J.; Zhao, D.; Lu, Y.; Wang, W.; Zhang, L.; Nishi, T. Natural rubber/nitrile butadiene rubber/hindered phenol composites with high-damping properties. *International Journal of Smart and Nano Materials* **2015**, *6*, 239–250.

(24) Johnson, T.; Thomas, S. Nitrogen/oxygen permeability of natural rubber, epoxidised natural rubber and natural rubber/epoxidised natural rubber blends. *Polymer* **1999**, *40* (11), 3223–3228.

(25) Davies, C. K. L.; Wolfe, S. V.; Gelling, I. R.; Thomas, A. G. Strain crystallization in random copolymers produced by epoxidation of cis 1,4-polyisoprene. *Polymer* **1983**, *24* (1), 107–113.

(26) Peng, L.; Li, Z.; Luo, W.; Li, Y. Analysis of dynamic viscoelastic properties of chloroprene rubber considering pre-strain effect. *Materials Research Express* **2019**, *6* (10), 105324.

(27) Nuyken, O.; Pask, S. D., 40 - Carbocationic Polymerization: Alkenes and Dienes. In *Comprehensive Polymer Science and Supplements*, Allen, G.; Bevington, J. C., Eds. Pergamon: Amsterdam, 1989; Vol. 3, pp 619–637.

(28) Wu, C.; Yamagishi, T.-A.; Nakamoto, Y.; Ishida, S.; Nitta, K.-h.; Kubota, S. Organic hybrid of chlorinated polyethylene and hindered phenol. I. Dynamic mechanical properties. *J. Polym. Sci., Part B: Polym. Phys.* **2000**, *38* (17), 2285–2295.

(29) Wu, C.; Yamagishi, T.-A.; Nakamoto, Y.; Ishida, S.-I.; Kubota, S.; Nitta, K.-h. Organic hybrid of chlorinated polyethylene and hindered phenol. II. Influence of the chemical structure of small molecules on viscoelastic properties. *J. Polym. Sci., Part B: Polym. Phys.* **2000**, *38* (11), 1496–1503.

(30) Li, J. C.; Zhang, H. S.; Zhao, X. Y.; Jiang, J. G.; Wu, Y. X.; Lu, Y. L.; Zhang, L. Q.; Nishi, T. Development of high damping natural rubber/butyl rubber composites compatibilized by isobutylene-isoprene block copolymer for isolation bearing. *Express Polymer Letters* **2019**, *13* (8), 686–696.

(31) Kennedy, J. Living cationic polymerization of olefins. How did the discovery come about? *Journal of Polymer Science Part A Polymer Chemistry* **1999**, *37* (14), 2285–2293.

(32) Kaszas, G.; Puskas, J. E.; Kennedy, J. Carbocationic copolymerization in the presence of electron pair donors. 2. Copolymerization of isobutylene and isoprene or 2,4-dimethyl-1,3-pentadiene with titanium tetrachloride-based initiating systems yielding in situ electron pair donors. *Macromolecules* **1992**, *25* (6), 1775–1779.

(33) Bochmann, M. Highly Electrophilic Organometallics for Carbocationic Polymerizations: From Anion Engineering to New Polymer Materials. *Accounts of chemical research* **2010**, *43* (9), 1267–1278.

(34) Cordoneanu, A.; Baird, M. C. Ultrahigh Molecular Weight Copolymers of Isobutene and 2,3-Dimethyl-1,3-butadiene Formed Using a Novel Protic Carbocationic Initiator, the 1:2 Adduct of n-Octadecanoic (Stearic) Acid and B(C₆F₅)₃. *Macromolecules* **2004**, *37* (18), 6744–6747.

(35) Zeldin, A.; Kukacka, L.; Fontana, J.; Carciello, N. Properties and structure of polymer concrete composite material with divinyl benzene as a crosslinking agent. *Polym. Compos.* **1981**, *2* (1), 1–7.

(36) Das, R.; Kumar, R.; Kundu, P. P. Vibration Damping Characterization of Linseed oil based Elastomers for its Effectiveness to Attenuate Structural Vibration. *J. Appl. Polym. Sci.* **2013**, *130* (5), 3611–3623.

(37) Sen, M.; Soydaş, O.; Aksüt, D. Preparation and characterization of high damping poly(epichlorohydrin) and poly(epichlorohydrin-co-ethylene oxide-co-allyl glycidyl ether) elastomers: I. Effect of curing system and blending on the damping properties. *React. Funct. Polym.* **2023**, *184*, No. 105520.

(38) Chugh, B.; Singh, A. K.; Thakur, S.; Pani, B.; Lgaz, H.; Chung, I.-M.; Jha, R.; Ebenso, E. E. Comparative Investigation of Corrosion-Mitigating Behavior of Thiadiazole-Derived Bis-Schiff Bases for Mild Steel in Acid Medium: Experimental, Theoretical, and Surface Study. *ACS Omega* **2020**, *5* (23), 13503–13520.

(39) Liang, Y.; Wang, H.; Li, J.; Wu, S.; Han, W.; Kang, H.; Fang, Q. Green Thermoplastic Vulcanizates Based on Silicone Rubber and Poly(butylene succinate) via In Situ Interfacial Compatibilization. *ACS Omega* **2021**, *6* (6), 4461–4469.

(40) Kapioti, K.; Matos, C. F.; Galembeck, F.; Jaillet, C.; Derré, A.; Zarbin, A. J. G.; Pénicaud, A. Highly Conducting, Sustainable, Nanographitic Rubber Composites. *ACS Omega* **2018**, *3* (2), 1367–1373.

(41) Martinez-Rubi, Y.; Ashrafi, B.; Jakubinek, M. B.; Zou, S.; Laqua, K.; Barnes, M.; Simard, B. Fabrication of High Content Carbon Nanotube-Polyurethane Sheets with Tailorable Properties. *ACS Appl. Mater. Interfaces* **2017**, *9* (36), 30840–30849.

(42) Wang, J.; Wang, M.; Zhang, X.; Han, Y.; Wu, Y.; Wang, D.; Qjn, X.; Lu, Y.; Zhang, L. Quantification Characterization of Hierarchical Structure of Polyurethane by Advanced AFM and X-ray Techniques. *ACS Appl. Mater. Interfaces* **2023**, *15* (38), 45388–45398.